





Oscillatory droplet dissolution from competing Marangoni and gravitational flows

Ricardo Arturo Lopez de la Cruz ^{1,*} Christian Diddens ¹,
Xuehua Zhang ^{2,1,†} and Detlef Lohse ^{1,3,‡}

¹*Physics of Fluids Group, Max-Planck-Center Twente for Complex Fluid Dynamics, and J. M. Burgers Centre for Fluid Dynamics, Faculty of Science and Technology, University of Twente, P.O. Box 217, 7500 AE Enschede, The Netherlands*

²*Department of Chemical and Materials Engineering, University of Alberta, Edmonton, Alberta, T6G 1H9, Canada*

³*Max Planck Institute for Dynamics and Self-Organization, Am Faßberg 17, 37077 Göttingen, Germany*



(Received 22 January 2022; revised 14 June 2022; accepted 26 August 2022; published 29 September 2022)

The dissolution or growth of a droplet in a host liquid is an important part of processes like chemical extraction, chromatography, or emulsification. In this work we look at the dissolution of a pair of vertically aligned droplets immersed in water, both experimentally and numerically. The liquids used for the droplets are long chain alcohols with a low but finite solubility in water and a significantly lower density than that of the host liquid. Therefore, a solutal plume is formed above of the bottom droplet and natural convection dominates the dissolution process. We monitor the volume of the droplets and the velocity field around them over time. When the liquids of the two droplets are the same, our previously found scaling laws for the Sherwood and Reynolds numbers as functions of the Rayleigh number [Dietrich *et al.*, *J. Fluid Mech.* **794**, 45 (2016)] can be applied to the lower droplet. However, remarkably, when the liquid of the top droplet is different than that of the bottom droplet the volume as function of time becomes nonmonotonic, and an oscillatory Marangoni flow at the top droplet is observed. We identify the competition between solutal Marangoni flow and density-driven convection as the origin of the oscillation and numerically model the process.

DOI: [10.1103/PhysRevFluids.7.094006](https://doi.org/10.1103/PhysRevFluids.7.094006)

I. INTRODUCTION

Droplet dissolution and more generally mass transfer between droplets and the surrounding liquid are important processes for varying technological applications. For instance, any process industry in which emulsions are part of the processes will be concerned with droplet dissolution. One example is within contactor columns where mass transfer can affect the coalescence of the droplets of the emulsion [1]. As another example, many foods and cosmetics are in the form of emulsions; thus stabilizing these emulsions is important for the shelf life of the products [2,3]. Yet another example is in the pharmaceutical industry where emulsions are used as a way to create drug delivery systems [4]. In environmental technology, the dissolution of CO₂ droplets deep in the ocean has been seen as a way to reduce the concentration of this gas in the atmosphere [5,6]. Finally, for chromatography the

*Corresponding author: ralcruz91@gmail.com

†Corresponding author: xuehua.zhang@ualberta.ca

‡Corresponding author: d.lohse@utwente.nl

mass transfer of a solute into a small droplet by liquid-liquid microextraction has been considered as a way to obtain high concentrations of the solutes needed [7–10].

Many efforts have been undertaken to better understand the diffusive dynamics of droplets; see an extensive discussion thereof in our reviews [11,12]. On the theoretical side the classical diffusion-based model for bubble dissolution of Epstein and Plesset [13] has been extended to the dissolution of spherical pure [14] and binary [15] droplets. Moreover, very recently, a more accurate binary droplet dissolution model was developed by Chu and Prosperetti [16] for the diffusion-dominated regime. Instead of approximating the equilibrium conditions of the dissolving entities at the interface, it explicitly makes use of the equality of chemical potentials and considers nonideal solutions, so that it could also be applied to translating droplets. Simultaneously, various experimental and numerical approaches for the dissolution of pure [17–27], binary [14,28] and multicomponent droplets [12,29,30] have been developed.

In the absence of an external flow, the dissolution of a droplet is purely determined by diffusion. The Epstein-Plesset-like model has been shown to be successful in capturing experimental observations for such pure diffusive situations [14]. However, once either forced or natural convection is present, models based on diffusion only obviously fail to properly predict the dissolution time of droplets [18,24,28]. Dietrich *et al.* [18] showed that when natural convection is present, a pentanol droplet submerged in water and with an initial radius of 0.7 mm takes 3 h to dissolve instead of the 11 h predicted by the Epstein-Plesset model. This was because of the emergence of a low-density plume of dissolved liquid on top of the droplet that accelerated the mass transport from the droplet into the host liquid. This process could quantitatively be modeled [18] and numerically be simulated [24].

When two or more droplets sit next to each other, their mutual interaction can affect the dissolution time [24,31,32]. Chong *et al.* [24] showed that when multiple droplets collectively dissolve in the purely diffusive regime, their dissolution time is increased because of shielding, as the dissolution of neighboring droplets reduces the concentration gradient experienced by the droplets. Moreover, if the droplets are arranged in a rectangular 3×3 lattice, due to shielding the central droplet takes longer to dissolve than those at the edges of the array. On the contrary, in the convective regime, the plumes created by each droplet can merge into one big centered plume, provided they are close enough, remarkably causing the dissolution time to be shorter than for a single droplet in the diffusive regime. But still the central droplet dissolves slower than those at the edges. Bao *et al.* [32] showed that if instead of natural convection there is an externally imposed flow, the dissolution of a lattice of droplets also displays the shielding effect and the droplets at the center of the lattice are the last to dissolve, while those which are upstream dissolve first. Additionally, it was shown that not unsurprisingly higher flow velocities and a larger spacing between the droplets resulted in shorter dissolution times.

Alongside the phenomena described so far, the presence of nonuniform temperature [23,33–36] and of concentration fields [37–39] can further complicate the dynamics of a dissolving droplet by giving rise to thermal and solutal Marangoni flows. If the droplet is not fixed in place, the forces caused by the Marangoni flow can propel the droplet against its own weight. Depending on the properties of the system, this can result in the droplets being suspended at a higher location than where a buoyancy balance would suggest or even more surprisingly make the droplet repeatedly jump [37]. In other cases, even without externally imposing a nonuniform field, the dissolution of the droplet can create gradients in concentration around itself that result in self-propulsion [25,40–44].

In the present work we study the simultaneous dissolution of two droplets in the natural convection regime. Different from the case of Chong *et al.* [24], one of the droplets is placed above the other, such that the plume caused by the lower droplet rises towards the upper one. In this way we further study the effects of convection on the dissolution of droplets, but also the effect of having solute already dissolved in the host liquid. Moreover, by changing the liquid of the upper droplet, gradients in the interfacial tension can arise, leading to some Marangoni flow that, as we will see, can become oscillatory.

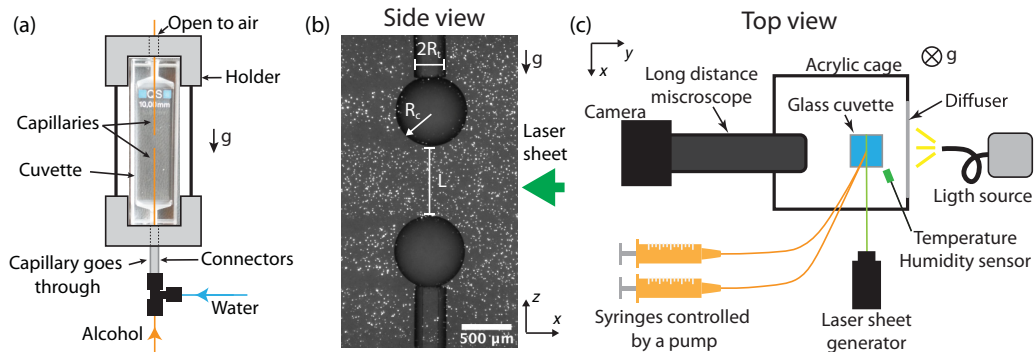


FIG. 1. (a) Sketch of the cuvette and the capillaries connected to it. (b) Typical example of two droplets just after infusion with tracer particles. The definitions of three length scales are shown. A laser sheet (parallel to the plane of the image) is coming from the right to illuminate the tracer particles. (c) Sketch of the experimental setup from a top view. The glass cuvette was illuminated from the back (from the right in the image) with a white light source. A diffuser was used to have an approximately homogenous illumination. The laser sheet illuminated the central plane normal to the direction of white light. A long distance microscope was used to observe the droplets. Each capillary was connected to a syringe pump. A cage of acrylic was built around the cuvette to reduce air currents and heat exchange with the surroundings. The cage was open from the top.

The paper is organized as follows: in the next section we describe our experimental methods and the numerical setup with its corresponding model equations. Afterwards, we present the experimental results of the dissolution of single droplets and pairs of vertically aligned droplets. For the latter case, we study the effect of changing the liquid of the upper droplet. For some cases there is an oscillatory flow which we study in more detail numerically. We then discuss the mechanisms behind the observed oscillatory flow. The paper closes with the conclusion and outlook section.

II. EXPERIMENTAL METHODS

A. Experimental setup

A cuvette (flow-trough cell, Suprasil quartz cuvette, Hellma) was used as a container; see Fig. 1(a). The cuvette had a square base and rectangular sides. The inner dimensions of the square were $10 \text{ mm} \times 10 \text{ mm}$. The total volume was $3300 \mu\text{l}$. Both at the bottom and at the top there were inlets through which two fused silica capillaries were inserted (Polymicro Technologies, nominal inner diameter $150 \mu\text{m}$, nominal outer diameter $360 \mu\text{m}$). In Fig. 1(a) we include a sketch of the capillaries and connectors. The capillaries have a polymer coating. We removed the coating close to the tips from where the droplets were infused, reducing the outer diameter to $320 \mu\text{m}$. The tips of the capillaries were slowly sanded to obtain an approximately flat end. The upper inlet of the cuvette was not sealed so that we could align the top capillary. Therefore, during the experiments a small amount of evaporation took place, normally in the order of $3 \mu\text{l}$ to $6 \mu\text{l}$ ($\sim 0.1\%$ the total volume).

Droplets of $0.2 \mu\text{l}$ were infused using glass syringes (Hamilton, $100 \mu\text{l}$, 1710 TLL, no stop) controlled by a syringe pump (Harvard Instruments, PHD 2000). An example of two droplets is shown in Fig. 1(b). For some experiments either the top or bottom capillary was removed in order to observe the dissolution of a single droplet.

The cuvette was held in front of a long distance microscope (Navitar $12\times$) and illuminated from behind with light that passed through a diffuser as depicted in Fig. 1(c). Videos were recorded with a charge-coupled device (CCD) camera (MD061MU-SY, Ximea). To measure the velocity field in

TABLE I. Properties of the liquids (at 25 °C) used in experiments. ρ is the density, D is the diffusion coefficient of the corresponding alcohol in water, c_{sat} is the saturation mass fraction of the alcohols in water, $\Delta\rho$ is the difference in density between pure water and water saturated with the alcohol, μ is the dynamic viscosity, γ is the interfacial tension with water, and $\partial\gamma/\partial c$ is the change in interfacial tension with mass fraction of pentanol as measured by the pendant droplet method [see the Supplemental Material (SM) [48]]. The initial Bond number $\text{Bo}_0 = gR_{e,0}^2\Delta\rho/\gamma$ is obtained for an initial equivalent radius $R_{e,0} = 363 \mu\text{m}$ and the density difference between pure water and the corresponding alcohol.

Liquid	ρ [$\frac{\text{kg}}{\text{m}^3}$]	D [$\frac{\text{mm}^2}{\text{s}}$]	c_{sat} [wt %]	$\Delta\rho$ [$\frac{\text{kg}}{\text{m}^3}$]	μ [mPa s]	γ [$\frac{\text{mN}}{\text{m}}$]	$\partial\gamma/\partial c$ [$\frac{\text{mN}}{\text{m}}$]	Bo_0
1-pentanol	811 ^a	888 ^b	2.2 ^c	3.42 ^a	3.52 ^d	4.4 ^e	–	0.05
1-hexanol	814 ^a	830 ^b	0.6 ^c	0.92 ^a	4.40 ^d	6.8 ^e	–11.7	0.03
1-heptanol	822 ^a	800 ^b	0.17 ^c	0.29 ^a	6.00 ^d	7.7 ^e	–20.4	0.03
1-octanol	827 ^a	780 ^a	0.049 ^c	0.07 ^a	7.60 ^d	8.52 ^e	–30.9	
Water	997 ^f	–	–	–	0.89 ^f	–	–	
Water saturated with pentanol	994 ^f	–	–	–	0.98 ^f	–	–	

^aObtained from Ref. [18].

^bObtained from Ref. [49].

^cObtained from Ref. [50].

^dObtained from Ref. [51].

^eObtained from Ref. [52].

^fObtained or extrapolated from Ref. [53].

the bath, a laser sheet was created using a La Vision system and a 532 nm laser of 0.1 W. The power was set between 53% and 57%, with the majority of the experiments at 55%. The width of the laser sheet was $310 \mu\text{m} \pm 70 \mu\text{m}$ during one set of experiments and $390 \mu\text{m} \pm 10 \mu\text{m}$ during a second set of experiments, measured using thermal paper and a calibrated picture of the mark. Fluorescent particles (Fluoro Max, red fluorescent polymer microspheres $6 \mu\text{m}$) were used to seed the flow with a concentration of 3×10^{-2} wt %. To confirm that the particles were faithful tracers we calculated their Stokes number $\text{St} = \tau_r U/R_{e,0}$, where $R_{e,0} = [3V_0/(4\pi)]^{1/3}$ is the equivalent radius of the droplet with initial volume V_0 . U is the characteristic velocity, either the velocity caused by Marangoni flows at the interface (obtained from simulations) or the velocity of the concentration plume. τ_r is the relaxation time of the tracer particles calculated as [29,37]

$$\tau_r \equiv \left(1 + \frac{\rho_{\text{sol}}}{2\rho_{\text{part}}}\right) \frac{d_{\text{part}}^2 \rho_{\text{part}}}{18\mu_{\text{sol}}}, \quad (1)$$

where ρ_{sol} and μ_{sol} are the density and dynamic viscosity of a saturated 1-pentanol in water solution. $\rho_{\text{part}} = 1050.00 \text{ kg/m}^3$ and $d_{\text{part}} = 6 \mu\text{m}$ are the density and diameter of the tracer particles. The calculated Stokes numbers are in the range of $\text{St} \sim 10^{-6}$ – $10^{-4} \ll 1$, meaning that indeed the particles are faithful tracers. The particle image velocimetry (PIV) analysis was carried out with the software PIVlab in Matlab using interrogation windows of $160 \mu\text{m}$ and $200 \mu\text{m}$ [45–47].

To reduce the thermal effects coming from the surroundings, a cage of acrylic panels was built around the cuvette, as shown in Fig. 1(c), and the experimentalist stood away from the setup once an experiment had started. The temperature and humidity around the cuvette were monitored with a sensor (HIH6130, Honeywell) placed a few centimeters away from the cuvette.

B. Liquids used

The bath consisted of Milli-Q water (produced by a Reference A+ system from Merck Millipore at 25 °C and $18.2 \text{ M}\Omega\text{cm}$). 1-Pentanol (ACS reagent $\leq 99\%$), 1-hexanol (reagent grade, 98%), 1-heptanol (98%), and 1-octanol (anhydrous $\leq 99\%$) were bought from Sigma-Aldrich and used as received. The properties of the liquids are listed in Table I.

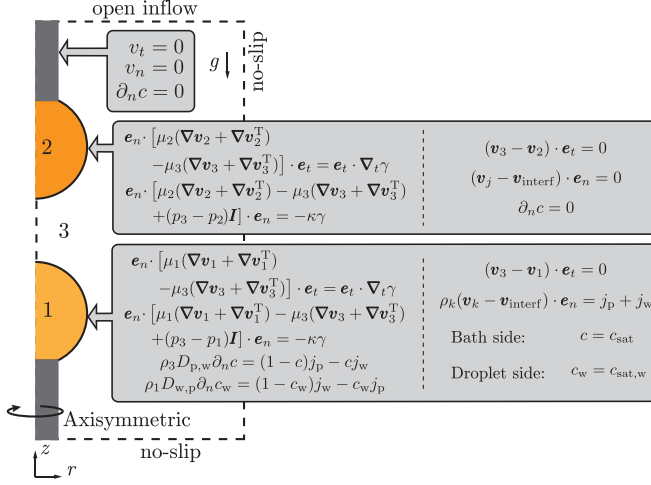


FIG. 2. Schematic of the numerical setup with the boundary conditions. The subscripts j and k take the values $j = 2, 3$ and $k = 1, 3$.

C. Experiment preparation

The capillaries were plasma-cleaned for 10 min before a set of experiments. After one experiment, about $0.5 \mu\text{l}$ of water was pumped to reduce the amount of pentanol dissolved. The water used in experiments was left at least 1 h in the laboratory before use. When a different liquid was used the cuvette was sonicated in a mixture of water and acetone for 10 min, then dried. The connectors were sonicated in water for 10 min and then also dried.

D. Numerical setup

We performed numerical simulations for the case of a 1-pentanol droplet at the bottom and a 1-octanol droplet at the top. We used a finite element method implemented on the basis of the finite element package OOMPH-LIB [54]. The liquids inside the droplets and the surrounding bath are discretized using triangular Taylor-Hood elements for the degrees of freedom of the velocity and pressure space, and a linear shape function for the composition in the three domains. The general numerical technique is described in detail in Ref. [55]; however, in that work the droplet was assumed to be a spherical cap while here the full interface dynamics are solved, thus the interface can deform and deviate from the shape of a spherical cap. Comparison with various experimental cases for benchmarking of the code can be found in [37,56,57].

The cylindrical symmetry of the system allows us to use an axisymmetric simulation as shown in Fig. 2. The chosen domain is cylindrical, 8 mm in height and 3 mm in diameter. Two solid cylinders are placed at the top and bottom along the axis of symmetry. As opposed to the experiments, the cylinders are not capillaries, thus the droplets are not connected to a reservoir of 1-pentanol. The base of the droplets is pinned to the cylinders. No-slip boundary conditions, a zero normal velocity, and no mass transfer were considered at the edges of the cylinders as depicted in Fig. 2.

The time stepping is done with the second-order backward differentiation formula with adaptive time steps based on the convergence of the Newton solver used, with a maximum time step of 0.1 s. Spatially, the system is discretized by around 100 000 degrees of freedom, with particular refinement near the interfaces, which turned out to be sufficient; i.e., finer discretizations do not yield noticeable differences.

Apart from the cylinders, the domain was divided into three regions: (1) the bottom droplet, (2) the top droplet, and (3) the bath. In the three regions we considered the continuity equation for

incompressible fluids and the Navier-Stokes with the Boussinesq approximation,

$$\nabla \cdot \mathbf{v}_\alpha = 0, \quad (2)$$

$$\rho_\alpha(\partial_t \mathbf{v}_\alpha + \mathbf{v}_\alpha \cdot \nabla \mathbf{v}_\alpha) = -\nabla p_\alpha + \nabla \cdot [\mu_\alpha(\nabla \mathbf{v}_\alpha + \nabla \mathbf{v}_\alpha^T)] - \rho_\alpha g \mathbf{e}_z, \quad (3)$$

where \mathbf{v}_α and p_α are respectively the velocity and pressure in each region $\alpha = 1, 2, 3$ and g the acceleration of gravity. The density and viscosity are functions of the mass fraction of 1-pentanol c , i.e., $\rho_\alpha = \rho_\alpha(c)$, and $\mu_\alpha = \mu_\alpha(c)$. The superscript T indicates the transpose. The reason behind the use of the Boussinesq approximation for the continuity equation lies in the numerics. While the complete equation considers density variation accurately, the partial masses are not perfectly conserved within the numerical scheme. However, when considering a divergence free fluid, this is not an issue, so we have decided to choose the Boussinesq approximation.

Inside the bottom droplet and the bath the advection diffusion equation is solved,

$$\rho_\alpha(\partial_t c + \mathbf{v}_\alpha \cdot \nabla c) = \nabla \cdot (\rho_\alpha D \nabla c), \quad (4)$$

where D is the diffusion coefficient of either pentanol in water (in the bath) or of water in pentanol (inside the lower droplet). Solving for either the mass fraction of 1-pentanol c (in the bath) or of water c_w (inside the droplet) is enough as they are coupled by the relationship $c_w + c = 1$. As a simplification, the top droplet is considered insoluble in water; thus there is no need to solve for the concentration inside the top droplet, and there is no third component going into the bath. The implications of this simplification will be addressed in the discussion section.

The boundary conditions for the tangential and normal stresses at the interfaces of both droplets are given by

$$\mathbf{e}_n \cdot [\mu_i(\nabla \mathbf{v}_i + \nabla \mathbf{v}_i^T) - \mu_3(\nabla \mathbf{v}_3 + \nabla \mathbf{v}_3^T)] \cdot \mathbf{e}_t = \mathbf{e}_t \cdot \nabla_t \gamma, \quad (5)$$

$$\mathbf{e}_n \cdot [\mu_i(\nabla \mathbf{v}_i + \nabla \mathbf{v}_i^T) - \mu_3(\nabla \mathbf{v}_3 + \nabla \mathbf{v}_3^T) + (p_3 - p_i)\mathbf{I}] \cdot \mathbf{e}_n = -\kappa \gamma, \quad (6)$$

where \mathbf{e}_n and \mathbf{e}_t are unit vectors in the normal and tangential direction with respect to the interface of each droplet. The symbol ∇_t indicates the gradient in the tangential direction. The subscript $i = 1, 2$ indicates that a quantity is inside the respective droplet. \mathbf{I} is the identity matrix, and κ is the curvature of the interface.

For both droplets the tangential velocities are continuous across the interface,

$$(\mathbf{v}_3 - \mathbf{v}_i) \cdot \mathbf{e}_t = 0. \quad (7)$$

Given that the top droplet is considered insoluble in water, no flux takes place across its interface, i.e., $\partial_n c = 0$, with ∂_n the partial derivative in the direction normal to the droplet interface. The resulting kinematic condition is

$$(\mathbf{v}_j - \mathbf{v}_{\text{interf}}) \cdot \mathbf{e}_n = 0, \quad (8)$$

where $\mathbf{v}_{\text{interf}}$ is the velocity of the interface and the subscript j is given by $j = 2, 3$ (see Fig. 2). On the contrary, the bottom droplet is allowed to dissolve. Therefore its corresponding kinematic condition is

$$\rho_k(\mathbf{v}_k - \mathbf{v}_{\text{interf}}) \cdot \mathbf{e}_n = j_p + j_w, \quad (9)$$

with $k = 1, 3$ (see Fig. 2).

The fluxes of 1-pentanol j_p and water j_w are also subject to the boundary conditions

$$\rho_3 D_{p,w} \partial_n c = (1 - c)j_p - c j_w, \quad (10)$$

$$\rho_2 D_{w,p} \partial_n c_w = (1 - c_w)j_w - c_w j_p. \quad (11)$$

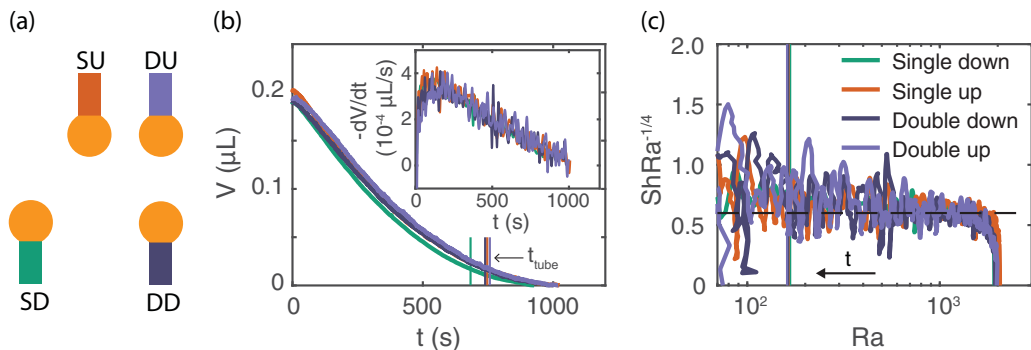


FIG. 3. Dissolution of pentanol droplets. (a) Diagrams showing the three configuration used in this figure. A single droplet down (SD), a single droplet up (SU), and double droplets down (DD) and up (DU). (b) Volume vs time of four pentanol droplets in the three configurations described in panel (a). Inset: Rate of volume change over time showing a local maximum. (c) Sherwood number compensated with $Ra^{-1/4}$ vs the Ra number. The horizontal dashed black line is a guide to the eye to compare with the data. Data with $Ra < 70$ have been omitted because the influence of the tube increases the noise significantly (the complete data set can be found in the SM [48]). The vertical colored lines in panels (b) and (c) indicate the time t_{tube} when the radius of curvature R_c is equal to the radius of the tubes R_t .

The concentrations at the interface were assumed to be the corresponding saturation values on both sides of the interface of the bottom droplet,

$$c_{\text{interf}} = c_{\text{sat}}, \quad \text{bath side}, \quad (12)$$

$$c_{\text{interf},w} = c_{\text{sat},w}, \quad \text{drop side}, \quad (13)$$

with the saturation values obtained from literature [50,58].

At the bottom and right edge of the domain we considered no-slip boundary conditions and no mass flux. Finally, an open inflow was assumed for the top edge.

III. RESULTS

A. Reference case: Dissolution of pentanol droplets

We first investigated the dissolution of pentanol droplets. We looked at the three different configurations shown in Fig. 3(a). In the first case we placed an individual droplet with the capillary below it, in the second case the capillary was above the droplet, and in the third case two droplets dissolved simultaneously, one above the other. The initial distance L_0 [see Fig. 1(a) for a definition] between the two droplets was $L_0 \sim 2R_{e,0}$, where $R_{e,0} = [3V_0/(4\pi)]^{1/3}$ is the initial equivalent radius, with $V_0 \sim 0.2 \mu\text{l}$ the initial droplet volume.

The droplet was assumed to be a spherical cap; thus to calculate its volume we fitted a circle to the edge of the two-dimensional projection of the droplet. The radius of the circle is the same as the radius of the spherical cap under the axisymmetric assumption. We found the intersection between the fitted circle and the edge of the capillary to determine the base of the droplet (the procedure is explained in more detail in the SM [48]). The deviation of the projected edge from a circle was small and only noticeable at the beginning. The initial Bond number $Bo_0 = gR_{e,0}^2\Delta\rho/\gamma$ for the droplets is much smaller than 1 as shown in Table I. Those small values are in agreement with only a small deformation of the droplet from the spherical cap shape. As dissolution takes place the radius and consequently the instantaneous Bond number become smaller, making the deviation from the spherical cap shape even smaller.

The experimentally observed volumes of the droplets for the three configurations are plotted in Fig. 3(b). There is no significant difference in the time evolution of the volume. While it seems that the single droplet at the bottom dissolves slightly faster than those of the other cases, the deviation is within our experimental error. In fact, from the inset in Fig. 3(b), it can be seen that the rate of change of the volume over time is essentially the same for the various cases. Therefore, the presence of a second droplet and the capillaries does not seem to considerably affect the dissolution process of the lower droplet.

To further characterize the dissolution of the droplets, we calculated the time-dependent solutal Rayleigh number and the time-dependent Sherwood number. The first one compares the time for mass transfer due to diffusion to the time of mass transfer due to natural convection and is calculated as [18]

$$\text{Ra}(t) = \frac{g\beta\Delta c_{m,i}R_e(t)^3}{\nu D}, \quad (14)$$

where ν is the dynamic viscosity of the bath (water at 25 °C), D is the diffusion coefficient of 1-pentanol in water, c_m is the concentration of solute in kgm^{-3} , and $\Delta c_{m,i} = c_{m,\text{sat}} - c_{m,\infty} = c_{m,\text{sat}}$ is the excess concentration at the interface with respect to the bath at infinity (assumed to be pure water) also in kgm^{-3} . The solutal expansion coefficient $\beta = (\partial\rho/\partial c_m)/\rho_{\text{water}}$ was obtained as $(\rho_{\text{sat}} - \rho_{\text{water}})/(c_{m,\text{sat}}\rho_{\text{water}})$, given that the density of the 1-pentanol–water solution as function of 1-pentanol concentration is approximately linear. The instantaneous equivalent radius was given by $R_e(t) = [3V(t)/(4\pi)]^{1/3}$ where $V(t)$ is the measured volume of the droplet.

The Sherwood number is the dimensionless mass transfer rate, calculated as [18]

$$\text{Sh}(t) = \frac{\langle \dot{m}(t) \rangle_A R_e(t)}{D\Delta c_{m,i}}. \quad (15)$$

The average mass flux $\langle \dot{m}(t) \rangle_A$ is calculated using the measured rate of change of the volume dV/dt as $\langle \dot{m} \rangle_A = \rho_p(dV/dt)/A(t)$ with ρ_p the density of 1-pentanol. $A(t)$ is the surface area of the droplet in contact with the bath, i.e., a spherical cap. $A(t)$ is calculated from the profile of the droplet.

Previously, it has been shown that the dissolution of sessile droplets with $\text{Ra} > 12$ is dominated by convection because of the formation of a plume above the droplet [18,24]. For the case of a thin thermal boundary layer with laminar flow, Bejan [59] showed that the Navier-Stokes equation within the Boussinesq approximation can describe the problem. Taking advantage of the correspondence between temperature and concentration, Dietrich *et al.* [18] applied the results by Bejan [59] to the solutal plume. For high Schmidt numbers $\text{Sc} = \nu/D$ ($\text{Sc} = 1105 \gg 1$ in our case), laminar quasisteady flow, and assuming constant pressure within the boundary layer, the balance between buoyancy and viscous drag give the scale for the width of the solutal boundary layer around the droplet as $\delta_c \sim R_e\text{Ra}^{-1/4}$. Furthermore, by considering that in the presence of convection δ_c is the relevant length scale for diffusion, the mass flux scales as $\langle \dot{m} \rangle_A \sim D\Delta c_{m,i}/\delta_c$ [18]. Finally, by introducing the scaling of δ_c and $\langle \dot{m} \rangle_A$ into the Sherwood number, the scaling law $\text{Sh} \sim \text{Ra}^{1/4}$ is obtained.

In Fig. 3(c) we have plotted the Sh number compensated by $\text{Ra}^{-1/4}$ vs the Ra number. We can see that after a transient time and while $\text{Ra} \gtrsim 100$, the group $\text{ShRa}^{-1/4}$ is approximately constant, indicating that indeed our system is dominated by convection, at least while the droplet is larger than the size of the capillary. The vertical colored solid lines in Figs. 3(b) and 3(c) indicate the time t_{tube} at which the radius of curvature is equal to the radius of the tube, $R_c = R_t$ [see Fig. 1(b)].

We have compared our data to the predictions of diffusion dominated models like the one of Epstein-Plesset [13], and indeed the dissolution times for those models are much larger than we observe experimentally, as expected from the value of $\text{Ra} \gg 12$ [18].

We have also measured the velocity field of the liquid surrounding the droplet. In Fig. 4(a) we show the velocity fields for the three configurations, with $L_0 \sim 2R_{e,0}$ for the double droplet case. Two times are shown, first a few seconds after the droplets were infused and later when the droplets are the same size as the capillary. In all cases there is the formation of a plume evidenced by the

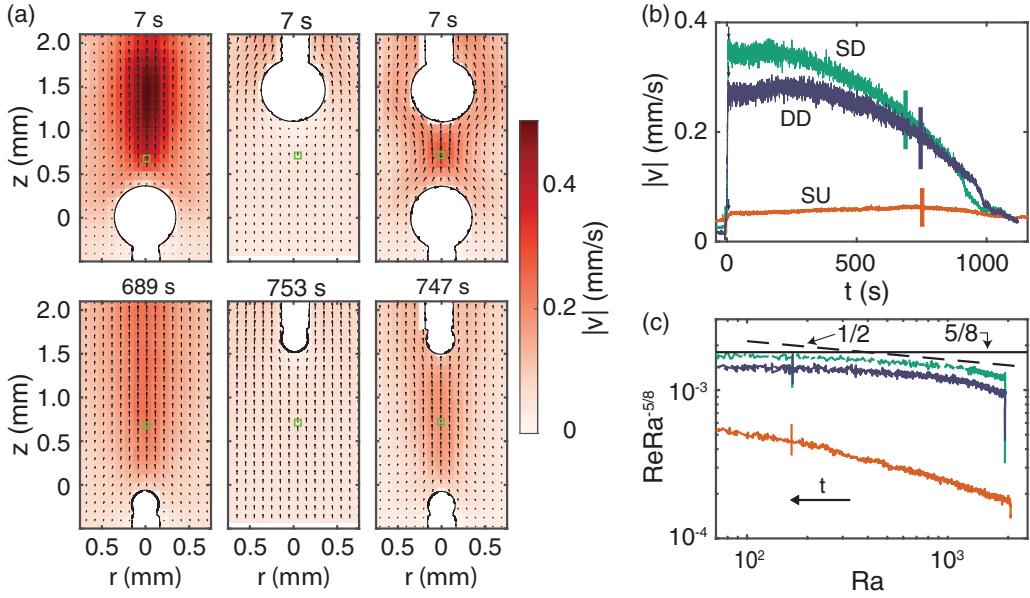


FIG. 4. Velocity caused by natural convection. (a) Velocity fields around the three different configurations. Two times are shown: 7 s after the droplets were infused (top) and when $t = t_{\text{tube}}$ (bottom). The velocity fields are averaged over a few frames, equivalent to $\Delta t = 1$ s. (b) Time evolution of the velocity measured at the axis of symmetry and approximately one initial radius away from the edges of the droplets. The locations where the velocity was obtained are marked with a small green square in the velocity fields of panel (a). The vertical black arrows indicate $t = 7$ s. (c) Reynolds number compensated with $\text{Ra}^{-5/8}$ vs the Ra number. The horizontal solid black line is a guide to the eye to compare with the data. The dashed black line corresponds to a power law of $1/2$. The vertical colored lines in panels (b) and (c) indicate $t = t_{\text{tube}}$. A plot with the complete range of Ra numbers can be seen in the SM [48].

higher velocity above the droplets (not shown for the SU case). For the SU case, the velocity in the region below the droplet is very small, indicating that the mass flux in the plume does not originate from below the droplet but from the sides. This partially explains why the dissolution process is not strongly affected by the presence of the upper droplet.

We measured the velocity over time at the axis of symmetry and about one initial radius away from the initial position of the edges of the droplets. Figure 4(b) shows the corresponding plot. The velocity first quickly goes up as the plume builds up (first ~ 6 s) and reaches an approximately constant value. However, eventually the velocity has to decrease as the droplet and its Rayleigh number become smaller. According to our data the velocity of the individual lower droplet is at first larger than in the double droplet case, but eventually they equalize. The initial difference must come from the obstacle effect that the upper droplet has, which forces the plume coming from the lower droplet to go around the upper droplet. We have also included the velocity measured one radius below the single upper droplet in Fig. 4(b). As already mentioned, the velocity is much smaller and is not very different from the existing background flow.

Dietrich *et al.* [18] also found a scaling law between the Reynolds number of the plume $\text{Re}(t) = v_{\text{plume}}(t)R_e(t)/\nu$ and the $\text{Ra}(t)$ number, with $v_{\text{plume}}(t)$ the velocity above the droplet and on the axis of symmetry. If as before we consider a thin boundary layer, quasisteady laminar flow, the Boussinesq approximation, and a constant pressure within the plume, it can be shown that the local width of the plume scales as $\delta_{c,\text{plume}}(z) \sim z[\text{Ra}(z)]^{-1/4}$, with $\text{Ra}(z) = [g\beta\Delta c_m(z)z^3]/(\nu D)$ the local

Rayleigh number. Additionally, from the advection diffusion equation, the scaling for the velocity can be obtained as $v_{\text{plume}} \sim D[\text{Ra}(z)]^{1/2}/z$ [18,59]. Considering mass conservation, the rate of transport of solute at the plume should be the same as the rate of dissolution of the droplet, meaning that $\dot{m} \sim \delta_{c,\text{plume}}^2(z)\Delta c_m(z)v_{\text{plume}}$. By combining this scaling relation for \dot{m} with the one obtained before, $\dot{m} \sim R_e^2 D \Delta c_{m,i} / \delta_c$ (considering that $A \sim R_e^2$), a scaling for $\Delta c_m(z)$ can be obtained. Notice that $\Delta c_{m,i} = c_{m,\text{sat}}$ is a constant while $\Delta c_m(z)$ depends on z . Finally, by introducing these scaling relations into the definition of the Reynolds number, the final result $\text{Re}(t) \sim \text{Ra}^{5/8}(t)\text{Sc}^{-1}$ is obtained.

In Figure 4(c) we have plotted the Re number compensated with $\text{Ra}^{-5/8}$ vs the Ra number in a double logarithmic plot. The group $\text{ReRa}^{-5/8}$ is not constant for all Ra numbers, indicating that there is not a pure power law. However, as Ra decreases, the compensated Re number tends to an approximately constant value, meaning that the data follow the same scaling as in Dietrich *et al.* [18] but only for an intermediate range of Ra numbers. Here the noise of our data is smaller because we do not have to take a derivative, therefore we can see the trend down to lower values of Ra, even after the droplet has reached the size of the capillary. We have also included a dashed black line corresponding to a power law of 1/2 as a second reference, showing that the data seem to follow a 1/2 power law for another range of Ra, which actually corresponds to about 500 s of the SU experiment. The discrepancy might come from the fact that v_{plume} is not constant for all values of z as obtained from the previous derivation [18]. Instead, in a plot of v_{plume} vs z , the velocity reaches a plateau only after a certain distance from the droplet, which can be seen as an approximately homogeneous color for $x = 0$ in the first two panels of Fig. 4(a). As the droplet becomes smaller, the plateau starts at lower values of z , in accordance with the fact that $\text{ReRa}^{-5/8}$ eventually tends to a constant value. Obviously, for the SU case the data do not follow the power law since there is no plume below the droplet.

It is important to notice that the plume is present up to the end of the life of the droplet because there is always 1-pentanol inside the capillary. The plume disappears only once some of the 1-pentanol inside the tube has dissolved. Therefore, we do not observe a strong Re number decrease at low Ra as opposed to Dietrich *et al.* [18].

B. Effect of changing the liquid of the upper droplet

With the dissolution of 1-pentanol droplets as a reference, we can now look at the effects of changing the liquid of the top droplet to 1-hexanol, 1-heptanol, or 1-octanol. In Fig. 5(a) we show that there is no effect in the volume evolution of the bottom droplet, as expected from the results of the previous section. The inset of Fig. 5(a) shows the nondimensional numbers based on the volume of the lower droplet. As before, for $\text{Ra} \gtrsim 100$ the group $\text{ShRa}^{-1/4}$ is approximately constant, while for lower values of Ra the variation in the Sh number are too large to see any clear trend. If we focus our attention to the time when the droplet is larger than the capillary, we can conclude that changing the liquid of the top droplet does not seem to affect the mechanism behind dissolution, namely, convection dominated dissolution.

On the contrary, as can be seen from Fig. 5(b), once the liquid of the top droplet is different from 1-pentanol, there is an initial increase in volume, more clearly seen for 1-heptanol and 1-octanol. This is an indication that some of the 1-pentanol that is transported by the plume dissolves into the upper droplet. To corroborate that this increase in volume is not a result of residual pressure in the tube, we looked at the dissolution in water of single droplets held at the top position. In the single droplet cases there can be indeed a small increase in volume at the beginning which is comparable with the increase observed in Fig. 5(b) for 1-hexanol. However, in the cases of 1-heptanol and 1-octanol the increase in volume of the single droplet case is considerably smaller than in the double droplet case, indicating that it must be a real effect and not an artifact caused by residual pressure. We show a comparison of the volume time series between the single and double droplet cases in the SM [48].

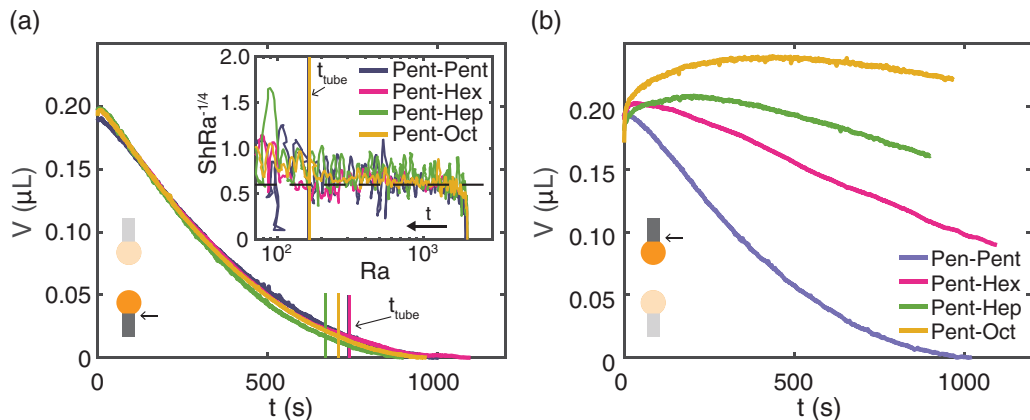


FIG. 5. Volume vs time for a 1-pentanol droplet dissolving below a second droplet of 1-pentanol or a different alcohol (1-hexanol, 1-heptanol, or 1-octanol). The initial separation is $L_0 \sim 2R_{e,0}$. (a) Volume of the lower droplet. The dissolution of the bottom pentanol droplet is hardly affected by changing the alcohol used for the upper droplet. Inset: Sh number compensated with $Ra^{-1/4}$ vs the Ra number, calculated with the volume of the lower droplet. For large values of the Ra the curve is approximately flat. The vertical colored lines in both plots indicate the time t_{tube} at which $R_c = R_l$. (b) Volume of the top droplet as function of time. When the top droplet is made of a different alcohol, it first increases in volume before it starts to dissolve. The diagrams in both panels (a) and (b) indicate the droplet from which the volume is plotted by the darker color and the arrows.

The upper droplet grows for a longer time the longer the carbon chain, as clearly shown by Fig. 5(b). The plausible explanation is the decreasing solubility of the alcohol with increasing length of the carbon chain (cf. Table I): the saturation concentration at the interface, and in turn the dissolution rate, will thus be smaller for a longer carbon chain. Since there is no alcohol of the top droplet already dissolved in the bath, dissolution must happen even if 1-pentanol is diffusing into the droplet. The volume change of the droplet will be given by the sum of both fluxes, and since the flux out is stronger for the smaller carbon chain, the volume increases only for a small time. However, as we will show next, there is a Marangoni flow at the top droplet taking place at the start of the dissolution process which could also affect the time over which the droplet grows in size.

In Fig. 6(a) we show the velocity measured one radius above the bottom droplet for the cases in which the liquid of the top droplet is changed from 1-pentanol to 1-octanol. Surprisingly, the velocity starts to oscillate once the 1-pentanol plume reaches the top droplet. In the inset of Fig. 6(a) we plotted only the first 100 s to better visualize the oscillations. Eventually, the oscillation stops and the velocity decreases over time.

The oscillatory behavior of the velocity is reminiscent of other oscillatory systems like the flows around droplets in a density-stratified bath [37,39], the up and down movement of a bubble inside a binary bath close to a heated surface [60], the periodic emission of plumes of a dissolving droplet [23,35,36], or the intermittent kicking of a pendant droplet of water surrounded by a binary gas [61]. Except for the pendant droplet case, in all the other systems just mentioned there is an imposed concentration or temperature gradient in the fluid surrounding the droplet, thus gradients of density and surface tension. The competition between these gradients drives the oscillatory flows. In the case of the pendant droplet surrounded by a gas, the gradients in surface tension and density come from the mass transfer from or to the droplet; nevertheless, these gradients are also the cause of the flow inside and outside the droplet. In our case, given that the 1-pentanol plume creates a gradient in concentration around the upper droplet, we can expect that a similar competition is at place in our experiments.

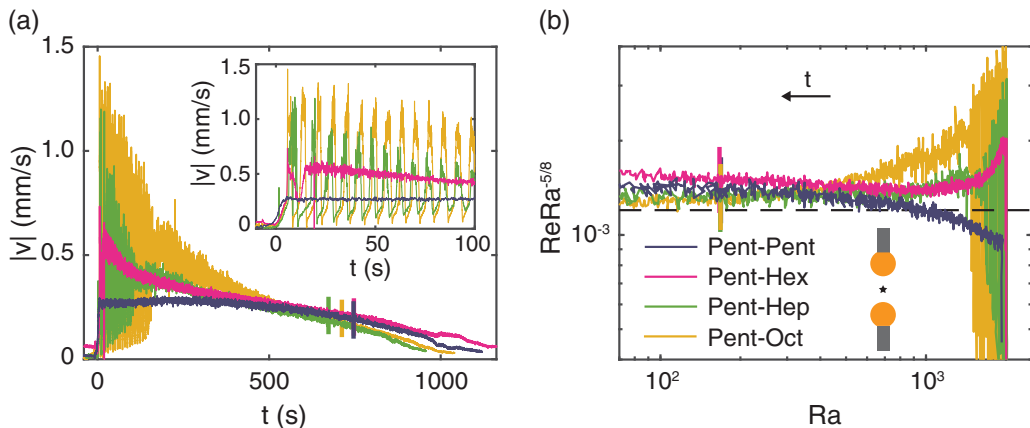


FIG. 6. Velocity-related data for pairs of droplets dissolving simultaneously with an initial separation of $L_0 \sim 2R_{e,0}$. (a) Velocity magnitude taken at the middle point between the two droplets. When the liquid of the upper droplet is not 1-pentanol the velocity temporarily oscillates once the plume created by the lower droplet reaches the upper droplet. Inset: Zoom of the first 100 s. During the oscillations, the velocity can reach more than 1 mm/s and then goes down to close to zero in each cycle. For the first cycles the vertical velocity can even become momentarily negative. (b) Reynolds number compensated with $Ra^{-5/8}$ vs the Ra number. In all cases, there is a region over which the data are approximately constant. The horizontal flat dashed line is used only as a reference. Inset: Sketch of the two droplets. The black star indicates the position where the velocity was measured. A plot with the complete range of Ra numbers is shown in the SM [48].

More precisely, when the plume touches the upper droplet, there is a local dip in the interfacial tension at the bottom of the top droplet. As a consequence, a Marangoni flow develops and pulls liquid from the bottom to the top of the droplet. We indeed see that the velocity suddenly increases in magnitude when the plume reaches the top droplet (see the SM [48] for movie 1). In the case of the jumping droplets in a stratified flow [37], the oil droplet suddenly jumps because of the Marangoni flow caused by the surrounding concentration gradient. Later, the same Marangoni flow causes the homogenization of the liquid inside the boundary layer around the droplet, stopping the Marangoni flow itself. Afterwards, the droplet moves down due to gravity until diffusion allows the far-field stratification to get in contact with the droplet once more, triggering the Marangoni flow again. In a similar way, one could assume that in our system the Marangoni flow transports the pentanol-rich liquid all around the droplet until a homogeneous layer is created around the top droplet. Later, the lower density of the pentanol-rich water as compared to pure water would advect the concentration boundary layer away, bringing the system to the initial state, where the plume could cause a concentration gradient along the interface. However, in the following section we will see, with the help of numerical simulations, that this view is slightly too simplistic and that in fact there is an extra step in which the lower plume detaches from the top droplet, and it is this step which actually causes the oscillatory behavior.

In Fig. 6(b) we show the corresponding compensated Re numbers as function of the Ra number. Again, the product $ReRa^{-5/8}$ is approximately constant for intermediate values of the Ra number, further suggesting that the $5/8$ scaling law becomes applicable only after the droplet dissolution process has been ongoing for some time.

IV. NUMERICAL SIMULATIONS OF THE OSCILLATORY REGIME

We simulated the case of a 1-pentanol down and a 1-octanol droplet up with an initial separation of $L_0 = R_{e,0}$ (notice that this is a smaller value of L_0 than in the previous section). In Appendix A

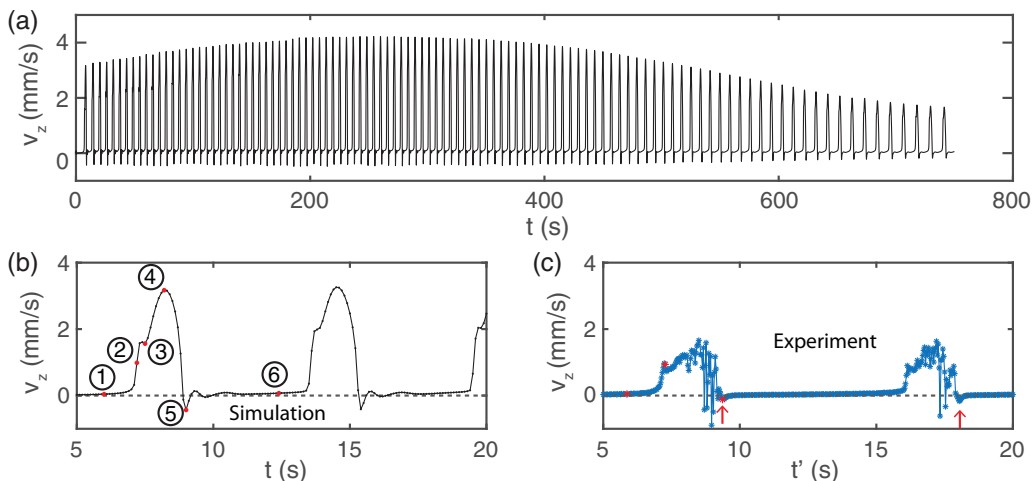


FIG. 7. Time series of the vertical velocity at the middle point between a 1-octanol droplet (top) and a 1-pentanol droplet (below). The numerical results are shown in panel (a) for the whole life time of the 1-pentanol droplet and in panel (b) for the first 20 s. The six times marked in panel (b) indicate the corresponding times of the snapshots shown in Fig. 8. The first 20 s of the experimental velocity are shown in panel (c). The experimental data were shifted horizontally to match the moment at which the velocity suddenly increases for the first time. The velocity fields corresponding to the red points in panel (c) are shown in Fig. 10. The initial separation between the edges of the droplets is $L_0 = R_{e,0}$ in all plots.

we show the velocity fields obtained from experiments and simulations at three different times, showing an overall good qualitative agreement, but with the velocity in simulations about twice as high as in experiments. Here we focus on the vertical velocity obtained at the middle point between the droplets. In Fig. 7(a) we have plotted the central velocity for the whole lifespan of the 1-pentanol droplet. From this plot it is clear that the oscillatory behavior of the velocity is satisfactorily recovered, and actually, as opposed to the experiments, it never stops. When we compare individual oscillation cycles, as shown in Figs. 7(b) and 7(c), it can be seen that the maximum velocity in both simulations and experiments are of the same order of magnitude, but, as already mentioned, with the velocity in simulations being about twice as high. On the contrary, the period of oscillation is longer in experiments, but again they both have the same order of magnitude. The differences could come from the fact that the diffusion into and from the upper droplet is turned off in the numerical simulations. However, the fair qualitative and to some degree even quantitative agreement lets us conclude that the diffusion into and from the upper droplet is not a key element for the appearance of the oscillatory behavior.

From the simulation, we can further verify the mechanism behind the oscillations proposed in the previous section. We have selected six different moments along the first oscillation cycle from the simulation, as marked in Fig. 7(b). The corresponding snapshots are shown in Fig. 8. The insets in each snapshot show plots of the interfacial tension vs s , a coordinate tangent to the interface of the upper droplet.

As we already concluded from experiments, initially [at time (1)] the dissolution of pentanol causes an accumulation of pentanol-rich liquid around the bottom droplet, which results in the creation of a convective plume. In the snapshot at time (1) the plume is just starting to move up, thus the surface tension along the surface of the top droplet is constant [see the inset at time (1)]. At time (2) the plume gets in contact with the top droplet creating a gradient in concentration along the interface, with the higher concentration at the bottom of the droplet. Therefore, as shown by the inset, the interfacial tension increases from the bottom towards the top of the droplet, and a

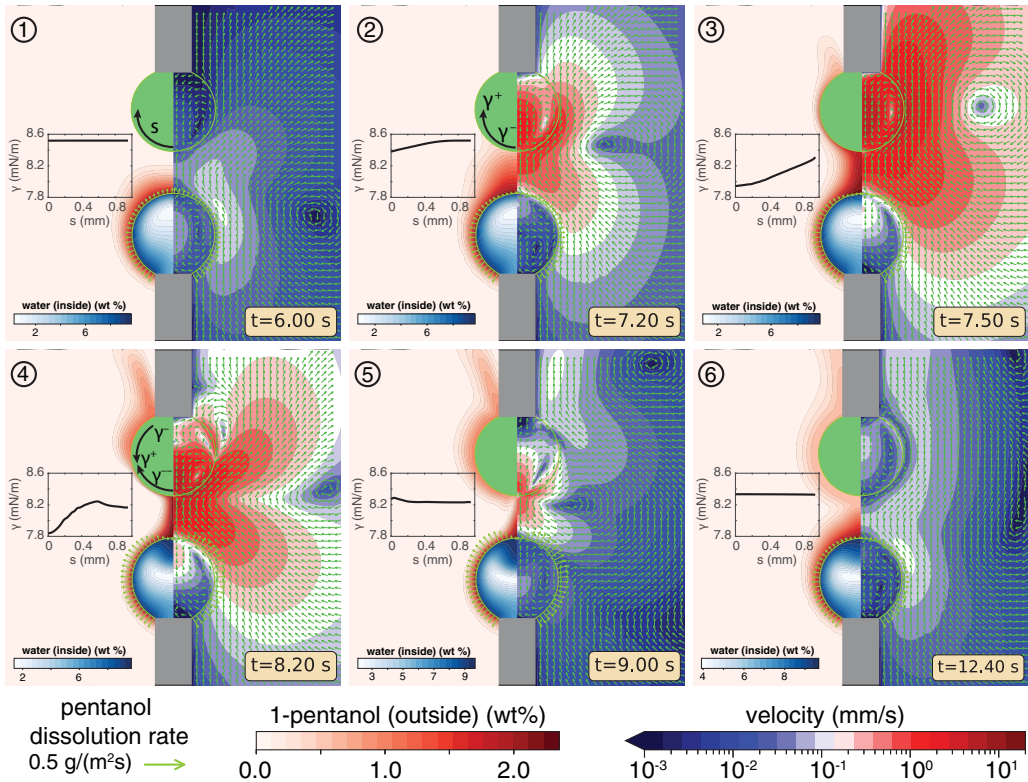


FIG. 8. Snapshots of the numerical results at six different moments during one oscillation cycle. At (1) the plume is building up and moves towards the top droplet. At (2) the plume has reached the top droplet, creating a gradient in interfacial tension and triggering an upwards Marangoni flow. At (3) the Marangoni flow has brought 1-pentanol rich liquid all around the droplet in a relatively thin concentration boundary layer. At (4) pentanol rich liquid has accumulated close to the contact line between the top droplet and the top capillary, causing a secondary Marangoni flow. At (5) the secondary Marangoni flow has created a thicker concentration boundary layer all around the droplet. The velocity at the axis of symmetry and in between the droplets points down, causing the plume to “detach” from the upper droplet. At (6) buoyancy competes with the secondary Marangoni flow. Eventually the plume is able to get in contact with the upper droplet again and the process restarts. The insets show the interfacial tension as a function of s , the coordinate tangential to the interface of the upper droplet.

Marangoni flow appears in the same direction. Just a fraction of a second later, at time (3), the positive gradient in interfacial tension and the Marangoni flow extend along the whole droplet interface, transporting the pentanol-rich liquid to the top of the droplet.

At the top of the droplet, the pentanol-rich liquid gets advected upwards but with a certain angle with the vertical axis due to the nonslip boundary condition at the wall of the capillary, which decelerates the flow. As a result, the concentration field takes the shape of a “horn” at the top of the droplet. Additionally, there is always the effect of gravity pulling up the pentanol-rich liquid. Both effects result on a thick region of pentanol-rich liquid on top of the droplet. Interestingly, within this thick concentration layer, the interfacial tension gradient changes in sign, which is evident from the inset at time (4) where there is a local maximum of the interfacial tension at an intermediate location along the interface of the droplet. As a consequence, an adversary Marangoni flow develops, transporting back down the pentanol-rich liquid and increasing the thickness of the concentration boundary layer from top to bottom. Notice that while the velocity caused by the primary Marangoni

flow is higher than that of the secondary flow, the secondary flow is able to propagate down by deflecting the primary flow to the side.

Eventually, the velocity along the interface of the top droplet completely reverses and the secondary Marangoni flow takes over [time (5)]. There is even a downwards flow between the two droplets, which pushes down the plume, away from the top droplet, letting the secondary Marangoni flow dominate. Notice that by bringing down pentanol-rich fluid and increasing the thickness of the concentration boundary layer around the upper droplet the result is similar to the homogenization caused by diffusion in the case of the bouncing droplet [37]. The homogenization is clearly seen by the almost constant value of the interfacial tension shown in the inset of snapshot at time (5).

Despite the downward flow caused by the secondary Marangoni flow, the pentanol-rich fluid is less dense than water, thus buoyancy eventually takes over, and, as shown in time (6), the flow starts to move upward once more. This causes that outside the top droplet and very close to its interface the velocity points down, but after a small distance it points up [look at the equator of the droplet at time (6) in Fig. 8]. Eventually, the plume is able to reach the top droplet again and the whole process repeats (see SM [48] for movie 2 showing more cycles throughout the life of the lower droplet). The inset at time (6) shows an almost constant interfacial tension. However, there is a very small negative gradient sustaining the downward flow.

When we look at our experiments, we can see that indeed there is a momentary downward flow at each cycle (at least for a few first cycles) in accordance with what we see in the simulations. We have pointed at the negative flow in Fig. 7(c) with red arrows. Additionally, Fig. 10(c) in Appendix A shows the experimental velocity field at the moment when the velocity between the droplets points down.

V. DISCUSSION

The secondary Marangoni flow starts once there is a thick layer of pentanol-rich liquid at the top of the droplet. One way to explain this phenomenon is to consider the concentration gradient normal to the interface of the droplet, $\partial_n c$. At the top, where there is a thick layer of concentrated liquid together with the “horn,” the gradient will be small. In regions around the equator of the droplet, the boundary layer is much thinner [see Fig. 8 at time (3)], thus $\partial_n c$ is large. This means that diffusion in the direction normal to the interface of the droplet is stronger at the regions where the concentration layer is thin. Eventually, this can cause that the concentration at a point of the interface within the thin layer region becomes smaller than the concentration at a point within the thick layer region.

One possible way to reduce the accumulation of pentanol-rich liquid at the top of the droplet is to change the nonslip boundary condition to a free-slip condition at the vertical wall of the capillary. Introducing this change in fact prevented the pentanol-rich liquid from being advected at an angle at the top of the droplet, but other than that the results were essentially the same (see the SM [48] for movie 4 showing a short video of this case). The fact that the pentanol-rich liquid has to travel upwards once it has passed the top droplet, either because of buoyancy or simply because of continuity, caused the widening of the concentration layer on the upper part of the droplet. Once this has happened, the mechanism proposed above can kick in and cause the reversal in the interfacial tension gradient.

It is possible that even without the capillary (and keeping the droplet in place somehow), the oscillatory behavior would still take place. In that case, once the pentanol-rich liquid has reached the top of the droplet, there would be a stagnation point at the top of the droplet, reducing the velocity caused by the Marangoni flow. This would allow buoyancy to affect the pentanol-rich liquid above the equator of the droplet and widen the concentration layer outside the upper half of the droplet. Moreover, if the Reynolds number were to be larger, and a pair of standing eddies were to appear behind the droplet, they would serve as a way to accumulate and mix the pentanol-rich solution on top of the droplet and trigger the secondary Marangoni flow.

As opposed to the experiments, in the simulation, the oscillations lasted for the whole life of the lower droplet. This suggests that some of the simplifications taken in the numerics play a role in

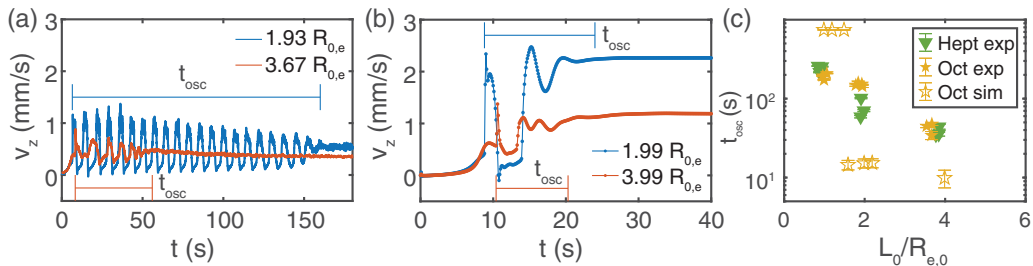


FIG. 9. Central velocity for (a) two experiments and (b) two simulations with different initial distances. (c) Time of oscillation t_{osc} vs the initial distance $L_0/R_{e,0}$ between the droplets, for 1-heptanol and 1-octanol in the top droplet in experiments and for 1-octanol in the top droplet in simulations. For the three smallest values of $L_0/R_{e,0}$ used in the simulations, the oscillations last for the whole life span of the pentanol droplet.

determining the time during which the oscillatory behavior is active. First of all, in the simulation we did not consider the dissolution of 1-pentanol into the 1-octanol droplet, which is clearly happening in experiments. At the same time, 1-octanol can also dissolve into the bath. Both mass transfer processes can affect the concentration at the interface and thus the Marangoni flow. Moreover, it is known that mass transfer of a solute that affects the interfacial tension can destabilize an interface [20,62–64]. Additionally, the liquids in the simulation are pure, while in experiments there can always be some contamination that could stop the flow. Some other possible effects that are not taken into account in the simulations are temperature variations, the presence of 1-pentanol inside the capillaries, and pressure perturbations coming from the capillaries and the syringes.

We have performed a few experiments and numerical simulations with different initial distances between the droplets, namely $L_0 \sim R_{e,0}$, $L_0 \sim 2R_{e,0}$, $L_0 \sim 4R_{e,0}$. In Figs. 9(a) and 9(b) we show experimental and numerical examples of the central velocity for two different values of L_0 with a 1-octanol droplet at the top. Clearly, by increasing the distance between the droplets the time over which the oscillations take place becomes shorter. In the simulations, increasing the initial distance dramatically reduced the oscillations to just a single complete oscillation, followed by a few weaker oscillations. In Fig. 9(c) we plotted the time of oscillation t_{osc} vs the initial length normalized by the initial radius $L_0/R_{e,0}$. t_{osc} is measured from the time the plume reaches the upper droplet (when the central velocity suddenly increases in magnitude) until the moment when the velocity becomes approximately constant within our experimental error. As already mentioned, the general trend is that the time of oscillation decreases with increasing $L_0/R_{e,0}$. This is possibly a consequence of a weaker concentration gradient in the plume, in both the axial and radial directions, because the plume travels for a longer distance. A smaller gradient results in a smaller Marangoni flow. Surprisingly, the time of oscillation in simulations has a sharp transition at a distance between $1.4R_{e,0}$ and $1.6R_{e,0}$. We do not have an explanation for this abrupt change, but this indicates that some of the simplifications taken in the simulations affect the time over which there are oscillations, apart from the initial separation distance $L_0/R_{e,0}$. We also measured the average oscillation period Δt . Interestingly, as shown in the SM [48], there is no significant change in the oscillation period with changing $L_0/R_{e,0}$ or by changing the liquid of the upper droplet from 1-octanol to 1-heptanol. As already observed, the simulations consistently show a smaller value of the oscillation period.

When the liquid is changed to a shorter carbon chain alcohol, the derivative of the surface tension with respect to the concentration of 1-pentanol ($\partial\gamma/\partial c$) is reduced (cf. Table I). As we saw in the previous section, oscillations did not happen when the top droplet was made of 1-pentanol, or they were very weak and for only a few cycles for 1-hexanol [see Fig. 6(a)], indicating that indeed a strong enough interfacial tension gradient is needed to produce oscillations. In Fig. 9(c) we can see that changing the liquid of the upper droplet from 1-octanol to 1-heptanol reduced the time of oscillation for the two larger values of $L_0/R_{e,0}$. However, for the smallest value of $L_0/R_{e,0}$ the

trend is reversed, indicating that it is a combination of $\partial\gamma/\partial c$, $L_0/R_{e,0}$, and other parameters not yet explored (like the solubility of the upper liquid), what sets the value of t_{osc} , with $L_0/R_{e,0}$ having a stronger effect than $\partial\gamma/\partial c$.

We have also tested numerically the case of a positive value of $\partial\gamma/\partial c$. In this case, since the interfacial tension increases with the concentration of 1-pentanol, the Marangoni effect causes liquid to move towards regions in the interface of high 1-pentanol concentration. Therefore, when the plume enters in contact with the top droplet the generated flow detaches the plume from the upper droplet. In general, the regions of high 1-pentanol concentration are repelled from the droplet, while in the situation discussed above the high-pentanol liquid was drawn towards the top droplet. Therefore, the resulting process is qualitatively different. A more detailed description of this case is presented in Appendix B.

Finally, as we discuss in the SM [48], changing the geometry at the contact line also seems to have an effect on the time of oscillation. Clearly, there are many parameters to be considered, but making an exhaustive exploration of the complete parameter space is beyond the scope of the present work.

VI. CONCLUSIONS AND OUTLOOK

We have studied the dissolution of droplets of alcohols, with carbon chains of different lengths, inside a water bath, mainly focusing on a system of two vertically aligned droplets dissolving simultaneously. As a reference case, we looked at the dissolution of an individual droplet of 1-pentanol and of two vertically aligned 1-pentanol droplets. We built up from these base cases and changed the liquid of the top droplet to alcohols with longer carbon chains. In all the cases, considering the dissolution of the lower droplet and the velocity of the plume, we recovered the scalings $Sh \sim Ra^{1/4}$ and $Re \sim Ra^{5/8}$, for an intermediate range of values of the Ra numbers used in this study. The scalings appear after an initial transient period and for large enough Rayleigh numbers, in particular, as long as the droplets are larger than the capillary used to hold them. This is in agreement with the results obtained previously for the dissolution of sessile droplets [18,24].

For two vertically aligned droplets, when the liquid of the top droplet was different from 1-pentanol, the interaction of the upper droplet with the 1-pentanol plume coming from below triggered an oscillatory Marangoni flow. During one cycle, the Marangoni flow pulls the liquid upwards, in the same direction as natural convection. However, the deflection of the flow at the top of the droplet, aided by buoyancy, causes the thickening of the concentration boundary layer on top of the droplet, resulting in an inversion of the concentration gradient along the interface of the droplet. Consequently, an adverse secondary Marangoni flow is triggered, which competes with the primary Marangoni flow and with natural convection. The secondary flow hinders the flow of the 1-pentanol plume coming from below and detaches the top droplet from the plume. Eventually buoyancy takes over and brings the plume back into contact with the upper droplet again.

By comparing our experimental and numerical results we could conclude that the diffusion of 1-pentanol into the top droplet and the dissolution of the top droplet into the bath do not play a prominent role in triggering the oscillatory behavior. However, mass transfer can affect the total duration of the oscillatory regime and causes a temporary increment in the volume of the top droplet. While the parameter space is large, we were able to recognize that for a larger spacing between the droplets the oscillatory behavior lasts less. A reduction on the value of the derivative of interfacial tension with respect to the concentration can also eliminate the oscillatory behavior. In future works, it would be interesting to further explore the parameter space by including more values of the initial distance L_0 between the droplets and of the initial radii of the droplets. It would also be instructive to change the density difference between the plume and the bath, and the viscosity of the liquids. In addition, it would be very interesting to see whether the oscillations persist if, for example, the capillary holds the upper droplet from the side and not from the top, or if in simulations the capillary is completely removed.

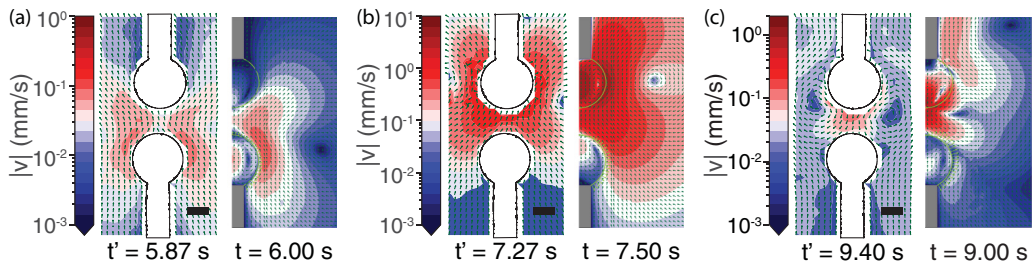


FIG. 10. Velocity fields obtained from experiments (left) and simulations (right) at three different moments during the first oscillation cycle: (a) before the plume reaches the upper droplet, (b) when there is a Marangoni flow all around the upper droplet, and (c) when the velocity between the droplets has changed direction. The scale bar represents $300 \mu\text{m}$. Notice that the color bars have different ranges in each panel. The times shown here correspond to red points in Figs. 7(b) and 7(c). Movies 2 and 3 in the SM [48] correspond to the simulated and experimental fields respectively.

ACKNOWLEDGMENTS

The authors thank A. Marin and many other members of the Physics of Fluids group for valuable discussions about the experimental setup and in particular Y. Li for a very insightful discussion on the mechanism behind the mixing caused by the Marangoni flow. This work was supported by the European Union (ERC-Advanced Grant Project DDD No. 740479 and ERC-Proof-of-Concept Grant Project No. 862032). X.H.Z. acknowledges support from the Natural Sciences and Engineering Research Council of Canada - Discovery Project (NSERC) and from the Canada Research Chairs program. There is no conflict of interest for this work.

APPENDIX A: VELOCITY FIELDS FROM EXPERIMENTS AND SIMULATIONS

To benchmark the numerical results we plot in Fig. 10 three velocity fields at three different times during the first oscillation cycle: Fig. 10(a) shows about 1 s before the plume reaches the upper droplet, Fig. 10(b) shows when the Marangoni flow is taking place over the whole surface of the upper droplet, and Fig. 10(c) shows when the velocity decreases in magnitude again and even changes direction. In general, the velocity obtained from the numerical simulations is higher than in experiments by a factor of approximately 2. However, the qualitative agreement is fairly good. More importantly, the simulation also shows the oscillatory behavior.

APPENDIX B: INCREASING SURFACE TENSION WITH RESPECT TO THE CONCENTRATION OF 1-PENTANOL

We performed one simulation for which the interfacial tension increased with increasing concentration of 1-pentanol, $\partial\gamma/\partial c = 30.9 \text{ mN/m}$, while the rest of the parameters were left unchanged. In a way, this is similar to swapping locations of the two droplets, but with the benefit of having a fast dissolution rate to create the plume, as opposed to actually locating the 1-octanol droplet below and the 1-pentanol droplet above. We summarize the results in Fig. 11.

The first observation is that the central velocity also oscillates over time, as evidenced by the plot shown in Fig. 11(a) for the whole life of the lower droplet and in Fig. 11(b) for the first 90 s. However, the situation is qualitatively different than in the case presented in the main text. Initially, the vertical velocity increases and decreases in an irregular way for approximately 50 s. Only then does the velocity follow an approximately periodic behavior with cycles that look very similar to those shown in the last 30 s of Fig. 11(b). In the long run, the amplitude of the oscillations decreases as shown by Fig. 11(a).

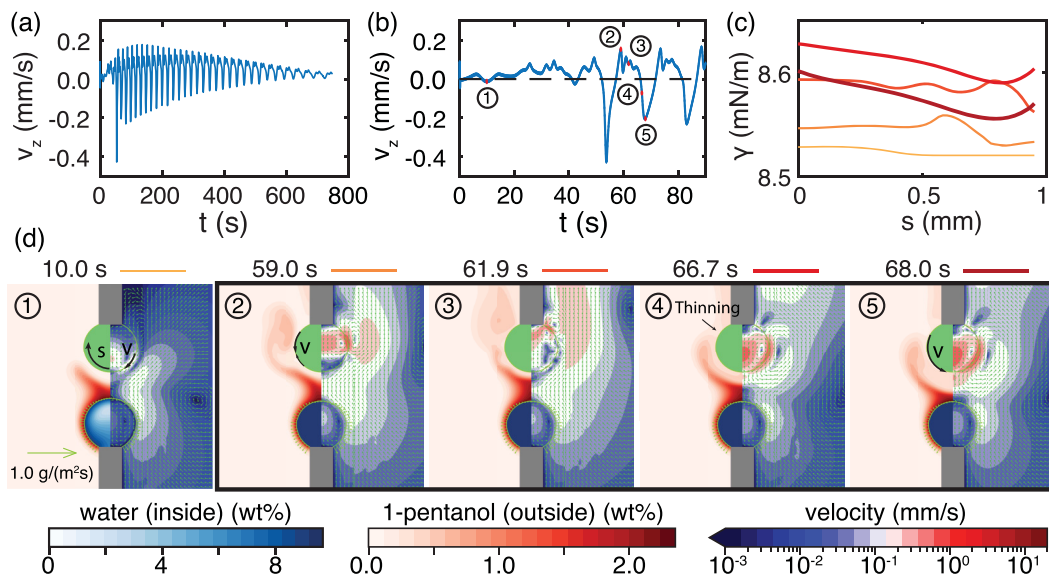


FIG. 11. Results from a numerical simulation of a 1-pentanol droplet below and a 1-octanol droplet on top, but the interfacial tension at the top droplet increases with increasing 1-pentanol concentration. The velocity measured at the middle point between the droplets for (a) the whole lifespan of the lower droplet and (b) for the first 90 s of the dissolution process. (c) The interfacial tension as function of the tangential coordinate s along the interface of the top droplet at five different times. (d) Five snapshots of the concentration and velocity fields at increasing times. The five times are marked in panel (b) with red points and correspond with the five curves in panel (c). The four snapshots inside the black rectangle correspond to different moments of a cycle.

Not surprisingly, when the pentanol-concentrated plume reaches the upper droplet, a negative interfacial tension gradient along the interface is generated. In Fig. 11(c) the plot at 10 s shows that the interfacial tension decreases as the tangential coordinate s increases, at least over a short range while it is approximately constant otherwise. As a consequence, the Marangoni effect drags liquid down along the interface of the upper droplet and towards the lower droplet. The downwards flow is strong enough to deviate the path of the plume as illustrated in the first panel of Fig. 11(d). The competition between the flow caused by the buoyant plume and the Marangoni flow explains the much smaller values of the central velocity, even smaller than the flow when the two droplets are made of 1-pentanol.

The deflected pentanol-rich liquid gets stretched to the sides by the flow and up by buoyancy, allowing the plume to reach the droplet from the sides. In the second panel of Fig. 11(d) we show how the partially separated part of the plume can “touch” the upper droplet at a point above its equator causing a maximum in interfacial tension at the contact point [see Fig. 11(c)]. Two opposing Marangoni flows appear towards the local maximum, which at that moment cause the central velocity to point up aiding the flow of the plume. Eventually, multiple “touching” points can be present at the same time [third panel of Fig. 11(d)] causing the interfacial tension and the interfacial velocity to have a periodic profile. Although the flow is complicated close to the interface, the pentanol-rich liquid that is far from the droplet continues to travel upwards and part of the plume is shed up. A region of low 1-pentanol concentration is formed between the plume and the region being shed, and this region gets thinner during the shedding process letting the pentanol-poor water get into contact with the upper droplet as shown in the fourth panel of Fig. 11(d). Therefore, a strong gradient in interfacial tension propagates over the whole droplet. The resulting Marangoni flow pushes the plume all the way down towards the lower droplet and stretches it to the sides [fifth panel of Fig. 11(d)]. From there, the process repeats.

We should note that in fact a weaker version of the process just described also takes place during the first 50 s (see the SM [48] for movie 5 showing the simulated velocity and concentration fields), but the Marangoni flow after the shedding is not as strong. Since the process is more evident at later times, we decided to show snapshots of those times. It is not entirely clear why the Marangoni flow becomes strong enough only after a few cycles, but we have noticed that it takes place after the lower droplet has reached the saturation concentration. More simulations with changes in the initial volume of the droplets or with different values of $\partial\gamma/\partial c$ could shed light on what determines the time at which the Marangoni flow becomes dominant. However, this is out of the scope of this work.

- [1] H. Groothuis and F. J. Zuiderweg, Influence of mass transfer on coalescence of drops, *Chem. Eng. Sci.* **12**, 288 (1960).
- [2] T. Zhang, J. Xu, Y. Zhang, X. Wang, J. M. Lorenzo, and J. Zhong, Gelatins as emulsifiers for oil-in-water emulsions: Extraction, chemical composition, molecular structure, and molecular modification, *Trends Food Sci. Technol.* **106**, 113 (2020).
- [3] V. Tchakalova, T. Zemb, and D. Benczédi, Evaporation triggered self-assembly in aqueous fragrance–ethanol mixtures and its impact on fragrance performance, *Colloids Surf. A* **460**, 414 (2014).
- [4] E. Lepeltier, C. Bourgaux, and P. Couvreur, Nanoprecipitation and the “ouzo effect”: Application to drug delivery devices, *Adv. Drug Delivery Rev.* **71**, 86 (2014).
- [5] P. G. Brewer, E. T. Peltzer, G. Friederich, and G. Rehder, Experimental determination of the fate of rising CO₂ droplets in seawater, *Environ. Sci. Technol.* **36**, 5441 (2002).
- [6] S. Hirai, K. Okazaki, Y. Tabe, K. Hijikata, and Y. Mori, Dissolution rate of liquid CO₂ in pressurized water flows and the effect of clathrate films, *Energy* **22**, 285 (1997).
- [7] A. Jain and K. K. Verma, Recent advances in applications of single-drop microextraction: A review, *Anal. Chim. Acta* **706**, 37 (2011).
- [8] M. Rezaee, Y. Assadi, M. M. Hosseini, E. Aghaee, F. Ahmadi, and S. Berijani, Determination of organic compounds in water using dispersive liquid–liquid microextraction, *J. Chromatogr. A* **1116**, 1 (2006).
- [9] M. Rezaee, Y. Yamini, and M. Faraji, Evolution of dispersive liquid–liquid microextraction method, *J. Chromatogr. A* **1217**, 2342 (2010).
- [10] D. Lohse, Towards controlled liquid–liquid microextraction, *J. Fluid Mech.* **804**, 1 (2016).
- [11] D. Lohse and X. Zhang, Surface nanobubbles and nanodroplets, *Rev. Mod. Phys.* **87**, 981 (2015).
- [12] D. Lohse and X. Zhang, Physicochemical hydrodynamics of droplets out of equilibrium, *Nat. Rev. Phys.* **2**, 426 (2020).
- [13] P. S. Epstein and M. S. Plesset, On the stability of gas bubbles in liquid-gas solutions, *J. Chem. Phys.* **18**, 1505 (1950).
- [14] P. B. Duncan and D. Needham, Microdroplet dissolution into a second-phase solvent using a micropipet technique: Test of the Epstein-Plesset model for an aniline–water system, *Langmuir* **22**, 4190 (2006).
- [15] J. T. Su and D. Needham, Mass transfer in the dissolution of a multicomponent liquid droplet in an immiscible liquid environment, *Langmuir* **29**, 13339 (2013).
- [16] S. Chu and A. Prosperetti, Dissolution and growth of a multicomponent drop in an immiscible liquid, *J. Fluid Mech.* **798**, 787 (2016).
- [17] E. Dietrich, E. S. Kooij, X. Zhang, H. J. W. Zandvliet, and D. Lohse, Stick-jump mode in surface droplet dissolution, *Langmuir* **31**, 4696 (2015).
- [18] E. Dietrich, S. Wildeman, C. W. Visser, K. Hofhuis, E. S. Kooij, H. J. W. Zandvliet, and D. Lohse, Role of natural convection in the dissolution of sessile droplets, *J. Fluid Mech.* **794**, 45 (2016).
- [19] J. M. Zhang, Y. Chen, D. Lohse, and A. Marin, Dissolution of microdroplets in a sparsely miscible liquid confined by leaky walls, *J. Fluid Mech.* **912**, A34 (2021).
- [20] N. M. Kovalchuk and D. Vollhardt, Marangoni instability and spontaneous non-linear oscillations produced at liquid interfaces by surfactant transfer, *Adv. Colloid Interface Sci.* **120**, 1 (2006).

- [21] J. T. Su, P. B. Duncan, A. Momaya, A. Jutila, and D. Needham, The effect of hydrogen bonding on the diffusion of water in *n*-alkanes and *n*-alcohols measured with a novel single microdroplet method, *J. Chem. Phys.* **132**, 044506 (2010).
- [22] T. Sato, R. Jung, and S. Abe, Direct simulation of droplet flow with mass transfer at interface, *J. Fluids Eng.* **122**, 510 (2000).
- [23] M. Lappa, C. Piccolo, and L. Carotenuto, Mixed buoyant-Marangoni convection due to dissolution of a droplet in a liquid–liquid system with miscibility gap, *Eur. J. Mech. B Fluids* **23**, 781 (2004).
- [24] K. L. Chong, Y. Li, C. S. Ng, R. Verzicco, and D. Lohse, Convection-dominated dissolution for single and multiple immersed sessile droplets, *J. Fluid Mech.* **892**, A21 (2020).
- [25] P. Poesio, G. P. Beretta, and T. Thorsen, Dissolution of a Liquid Microdroplet in a Nonideal Liquid-Liquid Mixture Far from Thermodynamic Equilibrium, *Phys. Rev. Lett.* **103**, 064501 (2009).
- [26] Q. Xie and J. Harting, The effect of the liquid layer thickness on the dissolution of immersed surface droplets, *Soft Matter* **15**, 6461 (2019).
- [27] S. Basu, D. C. K. Rao, A. Chattopadhyay, and J. Chakraborty, Dissolution dynamics of a vertically confined sessile droplet, *Phys. Rev. E* **103**, 013101 (2021).
- [28] E. Dietrich, M. Rump, P. Lv, E. S. Kooij, H. J. W. Zandvliet, and D. Lohse, Segregation in dissolving binary-component sessile droplets, *J. Fluid Mech.* **812**, 349 (2017).
- [29] H. Tan, C. Diddens, A. A. Mohammed, J. Li, M. Versluis, X. Zhang, and D. Lohse, Microdroplet nucleation by dissolution of a multicomponent drop in a host liquid, *J. Fluid Mech.* **870**, 217 (2019).
- [30] S. Maheshwari, M. Van Der Hoef, A. Prosperetti, and D. Lohse, Molecular dynamics study of multicomponent droplet dissolution in a sparingly miscible liquid, *J. Fluid Mech.* **833**, 54 (2017).
- [31] G. Laghezza, E. Dietrich, J. M. Yeomans, R. Ledesma-Aguilar, E. S. Kooij, H. J. W. Zandvliet, and D. Lohse, Collective and convective effects compete in patterns of dissolving surface droplets, *Soft Matter* **12**, 5787 (2016).
- [32] L. Bao, V. Spandan, Y. Yang, B. Dyett, R. Verzicco, D. Lohse, and X. Zhang, Flow-induced dissolution of femtoliter surface droplet arrays, *Lab Chip* **18**, 1066 (2018).
- [33] N. O. Young, J. S. Goldstein, and M. J. Block, The motion of bubbles in a vertical temperature gradient, *J. Fluid Mech.* **6**, 350 (1959).
- [34] E. Bassano, Numerical simulation of thermo-solutal-capillary migration of a dissolving drop in a cavity, *Int. J. Numer. Methods Fluids* **41**, 765 (2003).
- [35] M. Lappa and C. Piccolo, Higher modes of the mixed buoyant-Marangoni unstable convection originated from a droplet dissolving in a liquid/liquid system with miscibility gap, *Phys. Fluids* **16**, 4262 (2004).
- [36] M. Lappa, Oscillatory convective structures and solutal jets originated from discrete distributions of droplets in organic alloys with a miscibility gap, *Phys. Fluids* **18**, 042105 (2006).
- [37] Y. Li, C. Diddens, A. Prosperetti, K. L. Chong, X. Zhang, and D. Lohse, Bouncing Oil Droplet in a Stratified Liquid and Its Sudden Death, *Phys. Rev. Lett.* **122**, 154502 (2019).
- [38] Y. Li, C. Diddens, A. Prosperetti, and D. Lohse, Marangoni Instability of a Drop in a Stably Stratified Liquid, *Phys. Rev. Lett.* **126**, 124502 (2021).
- [39] K. Schwarzenberger, S. Aland, H. Domnick, S. Odenbach, and K. Eckert, Relaxation oscillations of solutal Marangoni convection at curved interfaces, *Colloids Surf., A* **481**, 633 (2015).
- [40] S. Michelin, E. Lauga, and D. Bartolo, Spontaneous autophoretic motion of isotropic particles, *Phys. Fluids* **25**, 061701 (2013).
- [41] C. C. Maass, C. Krüger, S. Herminghaus, and C. Bahr, Swimming droplets, *Annu. Rev. Condens. Matter Phys.* **7**, 171 (2016).
- [42] Z. Izri, M. N. van der Linden, S. Michelin, and O. Dauchot, Self-propulsion of Pure Water Droplets by Spontaneous Marangoni-Stress-Driven Motion, *Phys. Rev. Lett.* **113**, 248302 (2014).
- [43] P. G. Moerman, H. W. Moyses, E. B. van der Wee, D. G. Grier, A. van Blaaderen, W. K. Kegel, J. Groenewold, and J. Brujic, Solute-mediated interactions between active droplets, *Phys. Rev. E* **96**, 032607 (2017).
- [44] Y. Chen, K. L. Chong, L. Liu, R. Verzicco, and D. Lohse, Instabilities driven by diffusiophoretic flow on catalytic surfaces, *J. Fluid Mech.* **919**, A10 (2021).

- [45] W. Thielicke and E. J. Stamhuis, Pivlab—towards user-friendly, affordable and accurate digital particle image velocimetry in MATLAB, *J. Open Res. Softw.* **2**, e30 (2014).
- [46] W. Thielicke and E. J. Stamhuis, PIVlab—Time-resolved digital particle image velocimetry tool for MATLAB (2019), <https://www.mathworks.com/matlabcentral/fileexchange/27659-pivlab-particle-image-velocimetry-piv-tool-with-gui>.
- [47] W. Thielicke, The flapping flight of birds: Analysis and application, Ph.D. thesis, University of Gröningen, 2014.
- [48] See Supplemental Material at <http://link.aps.org/supplemental/10.1103/PhysRevFluids.7.094006> for a description of the image processing, error estimation in volume calculation and data cleaning; results on the dissolution of single droplets of 1-hexanol, 1-heptanol, and 1-octanol; results on the period of oscillation; a short discussion on the effect of the geometry of the contact line; measurements of the interfacial tension between the alcohols and water-pentanol mixtures; plots of the nondimensional groups versus the whole range of Ra numbers; information related to the supplementary movies.
- [49] L. Hao and D. G. Leaist, Binary mutual diffusion coefficients of aqueous alcohols. Methanol to 1-heptanol, *J. Chem. Eng. Data* **41**, 210 (1996).
- [50] K. Kinoshita, H. Ishikawa, and K. Shinoda, Solubility of alcohols in water determined the surface tension measurements, *Bull. Chem. Soc. Jpn.* **31**, 1081 (1958).
- [51] A. S. Al-Jimaz, J. A. Al-Kandary, and A. M. Abdul-Latif, Densities and viscosities for binary mixtures of phenetole with 1-pentanol, 1-hexanol, 1-heptanol, 1-octanol, 1-nonanol, and 1-decanol at different temperatures, *Fluid Phase Equilib.* **218**, 247 (2004).
- [52] A. H. Demond and A. S. Lindner, Estimation of interfacial tension between organic liquids and water, *Environ. Sci. Technol.* **27**, 2318 (1993).
- [53] Y. Pai and L. Chen, Viscosity and density of dilute aqueous solutions of 1-pentanol and 2-methyl-2-butanol, *J. Chem. Eng. Data* **43**, 665 (1998).
- [54] M. Heil and A. L. Hazel, oomph-lib—An Object-Oriented Multi-Physics finite-element Library, in *Fluid-Structure Interaction: Modelling, Simulation, Optimization*, edited by H.-J. Bungartz and M. Schäfer, *Lecture Notes in Computational Science and Engineering*, Vol. 53 (Springer, Berlin, 2006), pp. 19–49.
- [55] C. Diddens, Detailed finite element method modeling of evaporating multi-component droplets, *J. Comput. Phys.* **340**, 670 (2017).
- [56] C. Diddens, H. Tan, P. Lv, M. Versluis, J. G. M. Kuerten, X. Zhang, and D. Lohse, Evaporating pure, binary and ternary droplets: Thermal effects and axial symmetry breaking, *J. Fluid Mech.* **823**, 470 (2017).
- [57] Y. Li, C. Diddens, P. Lv, H. Wijshoff, M. Versluis, and D. Lohse, Gravitational Effect in Evaporating Binary Microdroplets, *Phys. Rev. Lett.* **122**, 114501 (2019).
- [58] A. F. M. Barton, Alcohols with water, in *Solubility Data Series*, edited by A. S. Kertes, Vol. 15 (Pergamon Press, Oxford, 1984), pp. 162–195.
- [59] A. Bejan, *Heat Transfer* (Wiley & Sons, NY, 1993).
- [60] B. Zeng, K. L. Chong, Y. Wang, C. Diddens, X. Li, M. Detert, H. J. W. Zandvliet, and D. Lohse, Periodic bouncing of a plasmonic bubble in a binary liquid by competing solutal and thermal Marangoni forces, *Proc. Natl. Acad. Sci. USA* **118**, e2103215118 (2021).
- [61] Y. Sutjiadi-Sia, P. Jaeger, and R. Eggers, Interfacial phenomena of aqueous systems in dense carbon dioxide, *J. Supercrit. Fluids* **46**, 272 (2008).
- [62] C. V. Sternling and L. E. Scriven, Interfacial turbulence: Hydrodynamic instability and the Marangoni effect, *AIChE J.* **5**, 514 (1959).
- [63] T. Köllner, K. Schwarzenberger, K. Eckert, and T. Boeck, Multiscale structures in solutal Marangoni convection: Three-dimensional simulations and supporting experiments, *Phys. Fluids* **25**, 092109 (2013).
- [64] K. Schwarzenberger, T. Köllner, H. Linde, T. Boeck, S. Odenbach, and K. Eckert, Pattern formation and mass transfer under stationary solutal Marangoni instability, *Adv. Colloid Interface Sci.* **206**, 344 (2014).